Title	Wall shear stress modified by bubbles in a horizontal channel flow of silicone oil in the transition region
Author(s)	Oishi, Yoshihiko; Murai, Yuichi; Tasaka, Yuji
Citation	International journal of heat and fluid flow, 86, 108748 https://doi.org/10.1016/j.ijheatfluidflow.2020.108748
Issue Date	2020-12
Doc URL	https://hdl.handle.net/2115/87262
Rights	© <2020>. This manuscript version is made available under the CC-BY-NC-ND 4.0 license https://creativecommons.org/licenses/by-nc-nd/4.0/
Rights(URL)	https://creativecommons.org/licenses/by-nc-nd/4.0/
Type	journal article
File Information	IJHFF2020_Oishi_fin.pdf

Wall shear stress modified by bubbles in a horizontal channel flow of silicone oil in the transition region

Yoshihiko Oishi[1]*, Yuichi Murai[2] and Yuji Tasaka [2]

[1] *Division of Production Systems Engineering, Muroran Institute of Technology,*
27-1 Mizumoto, Muroran, Hokkaido, 050-8585, Japan
[2] *Laboratory for Flow Control, Faculty of Engineering, Hokkaido University,*
N13W8, Sapporo, Hokkaido, 060-8628, Japan

* Corresponding author: Yoshihiko Oishi, E-mail: oishi@mmm.muroran-it.ac.jp

Abstract:

We performed laboratory experiments on bubbly channel flows using silicone oil, which has a low surface tension and clean interface to bubbles, as a test fluid to evaluate the wall shear stress modification for different regimes of bubble migration status. The channel Reynolds numbers of the flow ranged from 1000 to 5000, covering laminar, transition and turbulent flow regimes. The bubble deformation and swarms were classified as packing, film, foam, dispersed, and stretched states based on visualization of bubbles as a bulk void fraction changed. In the dispersed and film states, the wall shear stress reduced by 9% from that in the single-phase condition; by contrast, the wall shear stress increased in the stretched, packing, and foam states. We carried out statistical analysis of the time-series of the wall shear stress in the transition and turbulent-flow regimes. Variations of the PDF of the shear stress and the higher order moments in the statistic indicated that the injection of bubbles generated pseudo-turbulence in the transition regime and suppressed drag-inducing events in the turbulent regime. Bubble images and measurements of shear stress revealed a correlated wave with a time lag, for which we discuss associated to the bubble dynamics and effective viscosity of the bubble mixture in wall proximity.

Keywords: Bubbly flow, Drag reduction, Turbulent flow, Wall shear stress

1. Introduction

Reducing frictional drag for marine vessels by injecting bubbles is regarded as a feasible energy-saving technology, which was first reported by McCormick and Bahattacharrya (1973). In the subsequent half century, bubbly drag reduction (BDR) has been studied widely in physics and engineering, as reviewed by Ceccio (2010) and Murai (2014). Among various flow configurations, a horizontal channel flow is the most commonly used to parameterize the bubble dynamics in BDR. The use of channel flow allows high experimental accessibility in exploring the inner structure of the bubbly two-phase boundary layer. Comparability with the results of direct numerical simulations (DNSs) for channel flows (e.g. Kim et al., 1987; Vreman and Kuerten, 2014) has promoted understanding of the BDR mechanism. Many studies have been undertaken based on DNS extended to bubbly flows (Ferrante and Elghobashi, 2003, 2004, 2005, 2007; Lu and Tryggvason, 2007; Seo et al., 2010; Roghair et al., 2011; Ma et al., 2016; Asiagbe et al., 2017; Chahed et al., 2017; Joshi et al., 2017; Du Cluzeau et al., 2019; Lin et al., 2019). Although these studies revealed how turbulence is modified by the presence of bubbles, assumptions were made of the bubbles in various ways, such as them being pointwise, spherical, sparse, or deformable. Moreover, most of these approaches have limited coupling of bubbles to the liquid phase owing to the difficulty in handling full two-way interactions at high void fractions in the wall proximity. That is to say, DNS is limited in its applicability to a wide parametric range of bubble states. Non-DNS type computational fluid dynamics (CFD) simulations for BDR have been used in recent years based on the Euler–Euler model (Colombo and Fairweather 2016, Zhao et al., 2019), Euler–Lagrange model (Pang et al., 2014 and Rawat et al., 2019), volume-of-fluid model (Hao et al., 2019), level-set approach (Feng et al., 2017), and an improved homogeneous model (Pang et al., 2017). In these models, the physical interaction between bubbles and turbulence is treated with very strong assumptions.

To clarify the fluid physics of BDR, it is essential to undertake experimental studies and CFD simulations in parallel, thereby targeting common flow conditions. One of the barriers to this end is management of the contamination effect on bubble surfaces in water (Parkinson et al., 2008, Takagi and Matsumoto, 2011). Because H_2O has molecular polarity in its atomic arrangement, impurities from the molecular scale to micrometer-scale adhere to the bubble surface. Thus, it is necessary to model the contamination effect in CFD solvers; otherwise, precise control of contamination is required on experimental side (Winkel et al., 2004). Contamination adversely influences many types of bubble properties, such as surface tension, drag and lift coefficients, coalescence, and the mean bubble size in the boundary layer. The Marangoni effect from intermediately contaminated water further complicates the bubble dynamics (Fukuta et al., 2008; Aoyama et al., 2018). The contamination effect is an electrochemical action on the bubble surface, and its coupling with DNS for hundreds of bubbles is unrealizable. This issue has restricted DNS studies of BDR for a long time.

Considering the above-mentioned challenges, we used silicone oil as the liquid phase in the present study. The molecular formula of the silicone oil used is $[3CH_3\text{-O-Si}]\text{-}n[\text{Si-O-}2CH_3]\text{-}[\text{Si-O-}3CH_3]$, where n is the number of core molecular chains. Because there is little molecular polarity in the arrangement of atoms in this large molecule, dirt like dust in the oil is inert to the bubble surface and remain in the oil. This enables us to study bubble dynamics without interference from the effect of contamination. Such a system had been strongly requested by DNS researchers, who had succeeded in conducting various 3D bubbly two-phase flow simulations for clean bubbles (Kawamura and Kodama, 2002; Sugiyama et al., 2008). Their strategy was to first establish DNS for bubbly flows, and then take the effect of contamination into account. In addition, the surface tension of silicone oil is one third of that of water, which raises the capillary number or Weber number at low flow speeds. This allows the assessment of the role of bubble deformability, bubble breakup, and coalescence in BDR. Because the peak bubble size during BDR is determined by the balance between bubble fragmentation and coalescence, BDR performance mainly relies on the motion of highly deformable bubbles (Sanders et al., 2006; Park et al., 2019). Using silicone oil, we expect that our measurements will serve as an experimental database for DNS researchers to compare their results without worrying about contamination as first purpose.

Our second purpose in the study was to provide experimental data covering the transition regime from laminar to turbulent channel flows. This contributes to the fundamental question of how bubbles modify the laminar/turbulent boundary-layer structure and the transitional Reynolds number in channel flows. Because channel flows are categorized as a flow governed by a subcritical transition (analogous to a pipe flow), the amplitude of finite disturbance induced by pseudo-turbulence of bubbles determines the suppression or enhancement of liquid turbulence. DNS researchers have not yet succeeded in simulating the transitional Reynolds number because of the difficulty in exact numerical reproduction of individual bubble wakes and bubble–bubble interactions at high void fractions. In laminar shear flow, the effective viscosity of the bubbly layer influences the wall shear stress, and is a function of capillary number (Rust and Manga, 2002; Murai and Oiwa, 2008; Tasaka et al., 2015; Murai et al., 2015). For turbulent flows, bubbles form a spatial network and clusters inside the boundary layer, even at low void fraction (Oishi et al., 2019). This inserts a new rheological layer in the original boundary layer and alters the wall shear stress. For void fractions higher than 10% at high Reynolds number, void waves spontaneously emerge inside the boundary layer as a result of drag reduction (Park et al., 2016, 2018). This is attributed to a time lag between bubble swarms and the local wall shear stress. The key questions that we will address are how the time lag is determined in turbulent flow and whether this exists in laminar flow.

In this work, we quantitatively evaluated the effect of bubble deformation and the role of bubble swarms on drag reduction from laminar to turbulent regimes using silicone oil. We statistically analyzed the temporal variation of the local shear stress measured using a time-resolved wall shear-stress sensor. We then clarified the correlation between local bubble motion and turbulent structure by image processing of high-speed camera recordings synchronized with the shear-stress sensor. In Section 2, we provide details of the experimental equipment, measurement system, and image processing method for analyzing bubbles. In Section 3.1, we then classify the states of the bubbly flow observed. The wall frictional drag is evaluated in Sections 3.2 and 3.3, from which different mechanisms of drag modification corresponding are explained. After statistically summarizing the advection velocities of individual bubbles (Section 3.4), we discuss the time lag between the changes in local shear stress and the variation of the local void fraction in cases where drag reduction was obtained (Section 3.5).

2. Experimental Methods

2.1 *Experimental setup*

The experimental setup is illustrated in **Fig. 1**. It consists of a flow controller, a rectifier, a test section (horizontal rectangular channel with a height of 20 mm, width of 160 mm, and total length of 6000 mm), and a deaeration unit. Silicone oil (kinematic viscosity $\nu = 1.07\times10^{5}$ m^2/s, surface tension $\sigma = 21\times10^{-3}$ N/m) and air were used as the working fluid at laboratory temperature. The oil was circulated by the pump (Ebara, 80VNP52.2) and its flow rate was adjusted by controlling the input frequency of an inverter (Showa Instrument Information Co. Ltd., FT-03070), the output of which was sent to the pump. The base flow conditions were characterized by the bulk Reynolds number, which is defined as $Re = UH/\nu$, where U and H denote the bulk mean liquid velocity and the height of the channel, respectively. The available range of Re is 1000–5000. Air bubbles were injected into the horizontal channel from above via 140 capillary needles (inner diameter of 0.1 mm) that we set in a bubble injector mounted at 875 mm downstream from the inlet of channel by a compressor (Tokyo Keiso Co. Ltd., F04-108478). We note that the bubbles migrate near the upper wall and occupy this region with a boundary layer void fraction up to 50% and an area-based projection void fraction up to 90%, respectively, while the bulk void fraction of the channel flow is lower than 3%.

Bubble images were recorded using a high-speed digital video camera (Photron, Fastcam-Max 120K) from the top of the channel at a frame rate of 1000 fps and a shutter speed of 1/20,000 s. To obtain the shadow images of bubbles, a metal halide lamp (Photron, HVC) backlit the bubbles through a light-diffusing sheet. The depth of field for the camera lens (Nikon, Micro-Nikkor 105mm f/2.8) was set large enough at 450 mm. This optical setup provided a uniformly white background and sharp bubble shadows in the recorded images. The observation windows were set at two positions — $x/H = 15$ (upstream) and 45 (downstream) — from the bubble injection point, $x = 0$. All the other experimental specifications are summarized in **Table 1**.

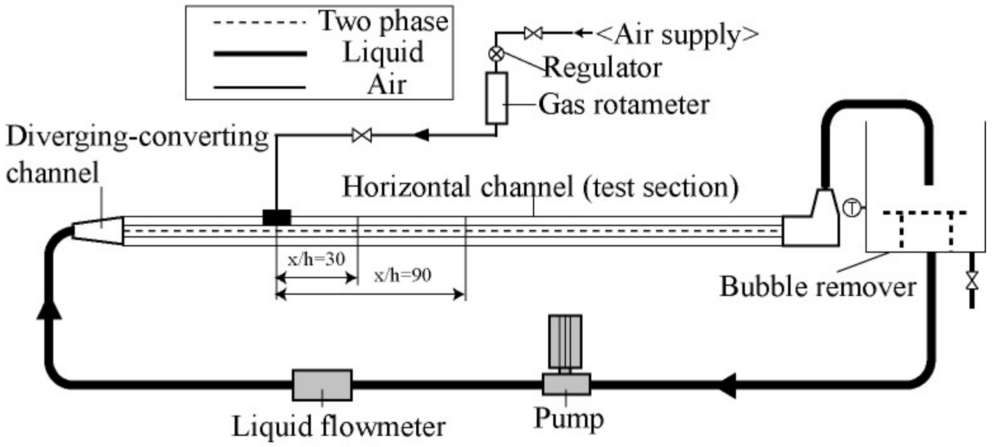

Fig. 1 Schematic diagram of the experimental setup.

Table 1 Experimental conditions

Main conditions			
Channel size	$H \times W \times L$	20 × 160 × 4000	mm
Channel height	H	20	mm
Bulk void fraction (Eq. (2))	α	0 to 3	%
Boundary layer void fraction (Eq. (3))	α_δ	0 to 50	%
Projection void fraction (Eq. (8))	β	0 to 90	%
Mean bubble diameter	d_{mean}	0.7	mm
Bulk liquid velocity	U	0.5, 1.0, 1.5, 2.0, 2.5	m/s
Bulk Reynolds number	$Re = HU / \nu$	1172 - 4665	
Working fluid: Silicone oil			
Density	ρ	935	kg/m^3
Kinematic viscosity	ν	1.07×10^{-5}	m^2/s
Temperature	T	20	deg.C
Surface tension	σ	21×10^{-3}	N/m
Camera conditions			
Measurement point	x/H	15, 45	-
Frame rate		1000	fps
Shutter speed		$1/(2.0 \times 10^4)$	s
Resolution		1024×1024	pixels
Sampling time		60	s

2.2 *Measurement of wall shear stress*

The wall frictional drag was obtained using a shear-stress sensor (SSK Co. Ltd., S10W-4; capacity: 3.9 mN; temporal resolution: 30 Hz) as a direct measurement of the wall shear stress. The head surface of the sensor with a 10-mm diameter was precisely set to be in the same plane as the top plate of the channel. This size of the sensor was much larger than the length scale of the turbulence, but can evaluate the local frictional drag with local void fraction fluctuating longer than the sensor size. Analog signal of the sensor was transferred to an analog amplifier (SSK Co. Ltd., M-1101), and then recorded on a PC via an A/D data recorder (Keyence Co., NR-500).

A schematic diagram of the measurement system is shown in **Fig. 2**. A pulse generator (Tabor Electronics Ltd., 50Hz, 8550) was used to synchronize the trigger of a high-speed camera and the data logger for the wall-shear stress sensor. The image acquisition position was 80 mm downstream from the measurement position of the wall shear stress because the devices could not be physically located at the same position. Hence, there was a time difference between the data obtained by each device. The time difference was removed using the local mean advection velocity of the bubble interface, which was measured using particle tracking velocimetry (PTV). The advection velocity of bubble has a relative velocity to the mean liquid velocity near the wall in the channel. At high void fractions, bubbles formed air films and moved faster than the liquid flow; for low void fractions, small bubbles moved slightly more slowly than the liquid flow. The data were analyzed based on the following dimensionless quantities.

The skin-friction coefficient, C_f, is defined by

$$C_\mathrm{f} = \frac{2\tau_\mathrm{w}}{\rho U^2}, \tag{1}$$

where τ_w, U, and ρ are the local wall shear stress measured by the shear-stress sensor, the bulk mean velocity of liquid phase in the channel, and the density of the oil, respectively. The bulk mean void fraction, α, is defined by

$$\alpha = \frac{Q_\mathrm{g}}{Q_\mathrm{l} + Q_\mathrm{g}}, \tag{2}$$

where Q is the volumetric flow rate, and the subscripts 'g' and 'l' indicate the gas and liquid phases, respectively. The boundary layer void fraction, α_δ, is estimated as

$$\alpha_\delta = \frac{Q_\mathrm{g}}{Q_\mathrm{l} + Q_\mathrm{g}} \approx \frac{Q_\mathrm{g}}{W\int_0^\delta u_y dy} \approx \frac{Q_\mathrm{g}}{WU\int_0^\delta \left(\frac{y}{\delta}\right)^{\frac{1}{7}} dy}, \quad \delta = \frac{1}{2}H \tag{3}$$

from the volumetric flow rates of the gas and liquid phases inside the turbulent boundary layer (Park et al., 2016, 2018). Here, u_y and δ are the vertical profile of the streamwise liquid velocity and thickness of the turbulent boundary layer, respectively. In this estimation, we applied the 1/7 power law of the boundary layer.

The bulk mean velocity in the two-phase conditions, U, was estimated taking the gas flow rate into account as

$$U = \frac{Q_\mathrm{l} + Q_\mathrm{g}}{HW} \tag{4}$$

where W denotes the channel width. Under two-phase conditions, the skin friction was evaluated using a fraction of the skin-friction coefficient in two-phase flow, C_f is modified by the following equation (Kodama et al., 2000; Murai et al., 2007):

$$\frac{C_\mathrm{f}}{C_\mathrm{f0}} = \frac{\tau_\mathrm{w}}{\tau_\mathrm{w0}} \frac{(1-\alpha)^2}{1-\alpha(1-\gamma)}, \tag{5}$$

where τ_w0 is the wall shear stress measured under single-phase flow, and the subscript '0' indicates the bubble-free condition; γ is the density ratio, $\rho_\mathrm{g}/\rho_\mathrm{l}$. In this study, the skin-friction ratio $C_\mathrm{f}/C_\mathrm{f0}$ was used to evaluate the modification of drag.

Bubble deformations in flows can be evaluated using the capillary number, *Ca*, under shear-dominant, steady conditions or using the Weber number, *We*, under inertia-dominant conditions. The capillary number is defined as

$$Ca = \frac{\mu_l G d}{2\sigma}, \tag{6}$$

where d, G, μ_l, and σ denote the bubble diameter, liquid velocity gradient, liquid viscosity, and the surface tension, respectively. *Ca* ranged from 0.1 to 0.5 under the experimental conditions of this study, indicating that bubbles were significantly deformed in the boundary layer. The definition of *We* is

$$We = \frac{\rho_l U^2 d}{\sigma}. \tag{7}$$

Bubbles break up when the effect of inertia is sufficiently larger than the effect of surface tension for Weber numbers larger than a critical value (We_c = 10). The bubbles in the present study underwent advection along the upper wall at a rate that depended on the velocity of the boundary layer, and were subjected to deformation and break-up owing to shearing. In our study, We = 104 for Re = 3732 and α = 1%; this value exceeded the critical value, meaning that bubbles largely deformed and broke up.

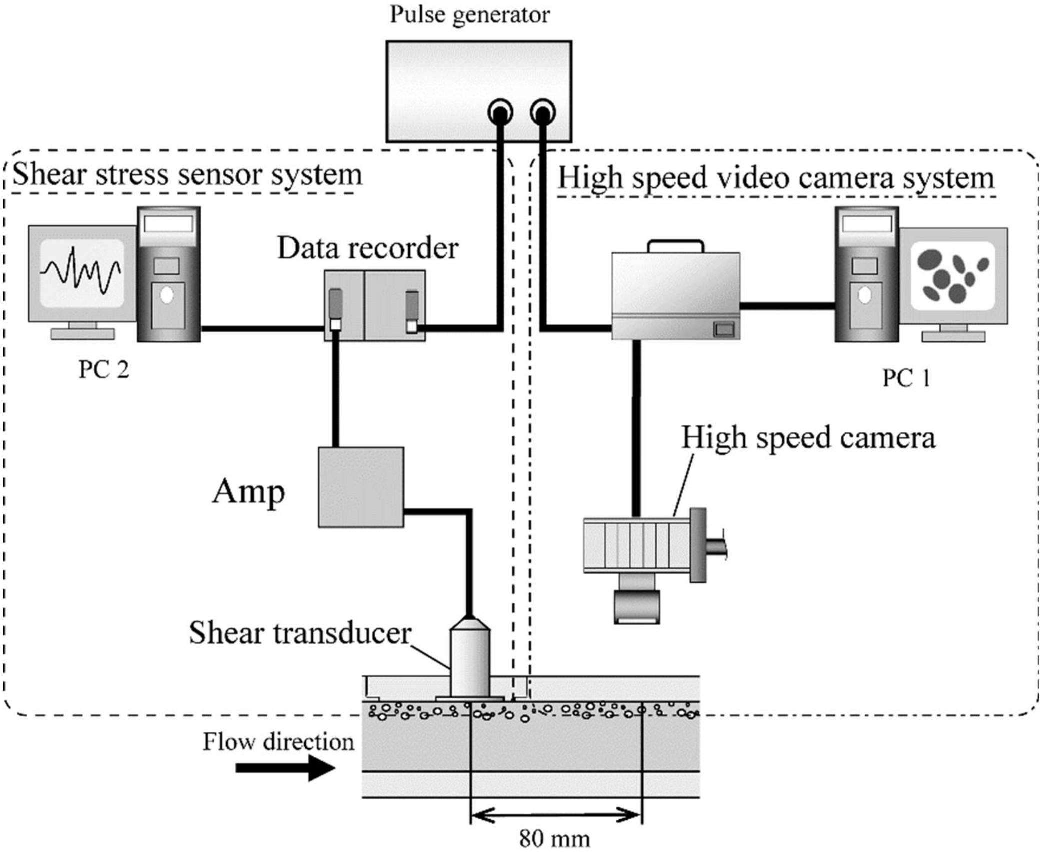

Fig. 2 Schematic diagram of the measurement system with synchronization of the shear-stress sensor and high-speed video camera for simultaneous measurement of local shear stress and local void fraction.

2.3. *Image processing for identifying sliding bubbles*

The process of image analysis for obtaining the local void fraction is shown in **Fig. 3**. Original images taken by the high-speed video camera (**Fig. 3(a)**) were processed via background subtraction, edge detection, binarization, thinning of the bubble outline (**Fig. 3(b)**), and the hill–holes process (**Fig. 3(c)**). The background-subtraction process removed the low-level noise of the primary image and normalized the whole pixels of the image. Edge detection highlighted the interfaces of the bubbles, and binarization and thinning processes extracted the bubble interfaces. The hill–holes process was used on a binary image to calculate projection void fraction to quantify the fluctuations of bubbles that slid on the wall surface. The projection void fraction is defined by

$$\beta = \frac{A}{B}, \tag{8}$$

where A is the total bubble-occupying area in the measurement area, B (Murai et al., 2001). We set B as a circular shape of a diameter of 10 mm, corresponding to the size of the wall shear stress sensor. The field of view was 53.8 mm × 53.8 mm in the spanwise and streamwise directions, and the image resolution was 1024 pixels × 1024 pixels. The corresponding image magnification factor was 53 μm/pixel. Image processing was performed using consecutive images longer than 4000 sequential frames under each experimental condition.

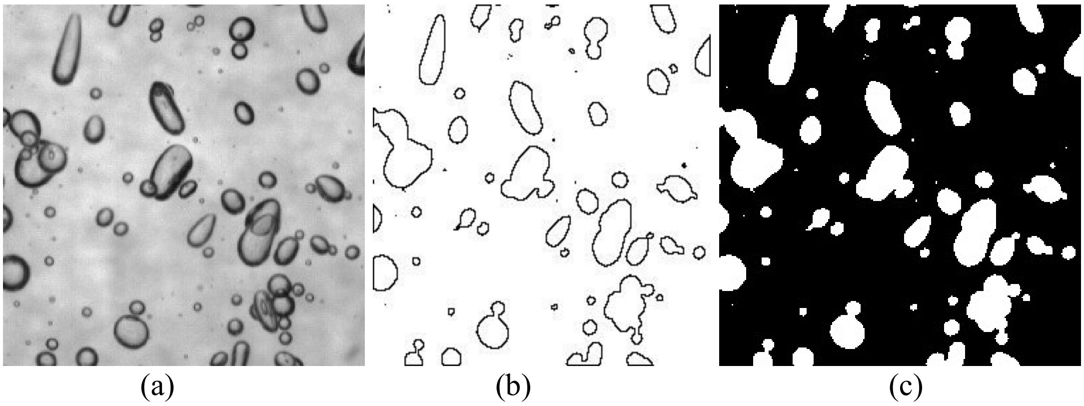
(a) (b) (c)

Fig. 3 Image analysis of the backlit projection of bubbles: (a) original image, (b) thinning image, and (c) binary image after processing the hill-photographs to measure the projection void fraction.

3. Results and Discussion

3.1 *Classification of bubble distribution*

In channel flow using silicone oil, bubbles are subjected to high viscous shear stress but low surface tension. A viscosity approximately 10 times larger than water and surface tension of one third of that of water result in high deformability of bubbles, even under low-speed conditions. **Figure 4** shows a snapshot of bubbles in the channel at a speed of $U = 0.5$ m/s and a bulk void fraction of $\alpha = 2.0\%$. Bubbles are distributed as swarms, with a certain spanwise spacing. In highly concentrated swarms, an air film forms owing to bubble coalescence. As a result, bubble-free regions often appear on the top wall of the channel.

Figure 5 shows photographs of the local instantaneous bubble distributions for different combinations of U and α. Each photograph was taken from the top at $x/H = 45$, where bubbles move from left to right. The flow without bubbles is between the laminar channel flow at $U = 0.5$ m/s ($Re = 1172$) and fully developed turbulent flow at $U > 2.0$ m/s ($Re > 3732$). Focusing on the photographs of the four corners in the figure, the bubbles can be classified into four patterns. At the slowest speed and lowest void fraction (top-left corner), spherical bubbles are tightly arranged. These bubbles are in contact with each other and are close to the two-dimensional packing limit. We name this the packing state. In the bottom-left corner (i.e. increasing the void fraction), bubbles form foams in which a honeycomb-like liquid film appears on the wall surface. We name this the foam state. The foam transits to many air films as the flow speed increases (bottom-right corner). This transition happens because of the high shear rate that breaks the liquid films in the foam. We name this the film state. Finally, at the highest speed and lowest void fraction (top-right corner), the gas phase is distributed as a dispersed state.

We note that long bubbles stretched in the streamwise direction at $U = 1.5$ m/s. We consider this to be a representative feature of bubbles owing to low surface tension in the silicone oil. Namely, the capillary number can increase to a high value before reaching the critical Weber number for bubble break-up. We name this the stretched state. All other bubble distribution patterns are intermediates of these four states.

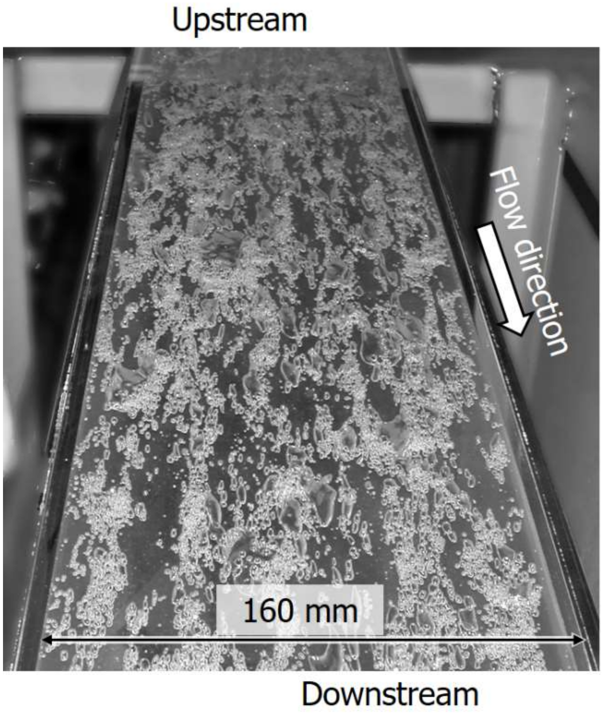

Fig. 4 Snapshot of bubbles in the silicone-oil channel flow at $U = 0.5$ m/s and $\alpha = 2.0\%$.

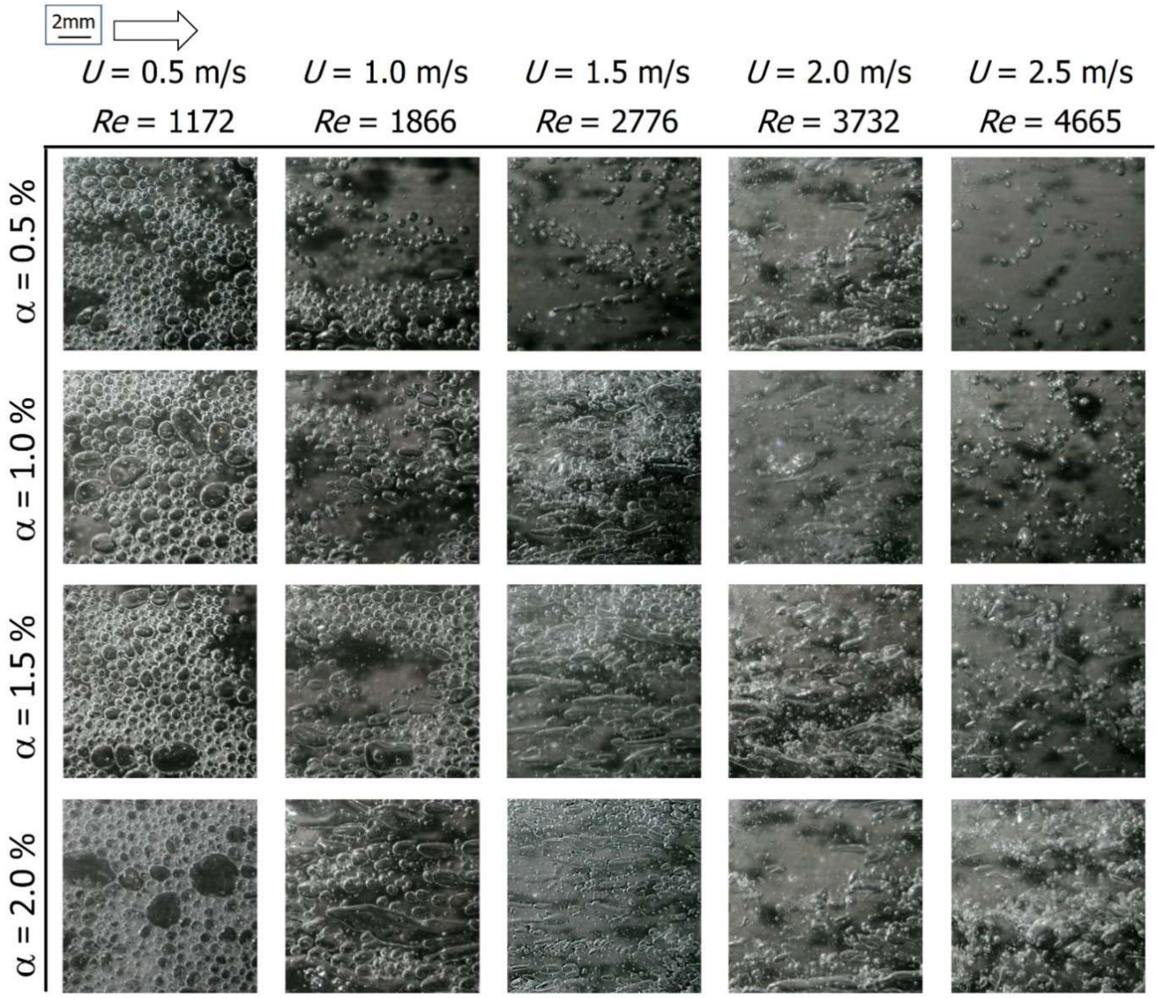

Fig. 5 Top-view photographs of local instantaneous bubble distributions taken at $x/H = 45$.

3.2 *Time-averaged wall shear stress*

We measured the wall shear stress of the top surface of the channel for five Reynolds numbers, six void fractions, and two downstream locations, thus 60 conditions in total. The results are summarized in **Fig. 6** as the local skin-friction coefficient, C_f. The two curves in the graph are the theoretical values of single-phase flow in laminar channel flow ($C_\mathrm{f} = 6 / Re$) and the empirical equation by Dean (1978) for fully developed turbulent channel flow ($C_\mathrm{f} = 0.073Re^{-1/4}$). At the location of $x/H = 15$ (**Fig. 6(a)**), injection of bubbles resulted in a large friction under all conditions at $Re < 3000$. In particular, at $Re < 2000$, C_f jumps up beyond value of single-phase turbulent flow. We attribute this to the effective viscosity of bubbles, which becomes very large in the packed and foam states. When the flow speed was increased up to $Re = 3732$, this effect was diminished since the high viscous oil was separated from the wall surface. In the downstream region at $x/H = 45$ (**Fig. 6(b)**), the general trend was similar to that of the upstream region. One notable difference is that the decrease in C_f was lower than that predicted using Dean's formula at $Re > 2000$. This infers the partial suppression of turbulence due to bubbles; this condition could be interpreted as partial re-laminarization.

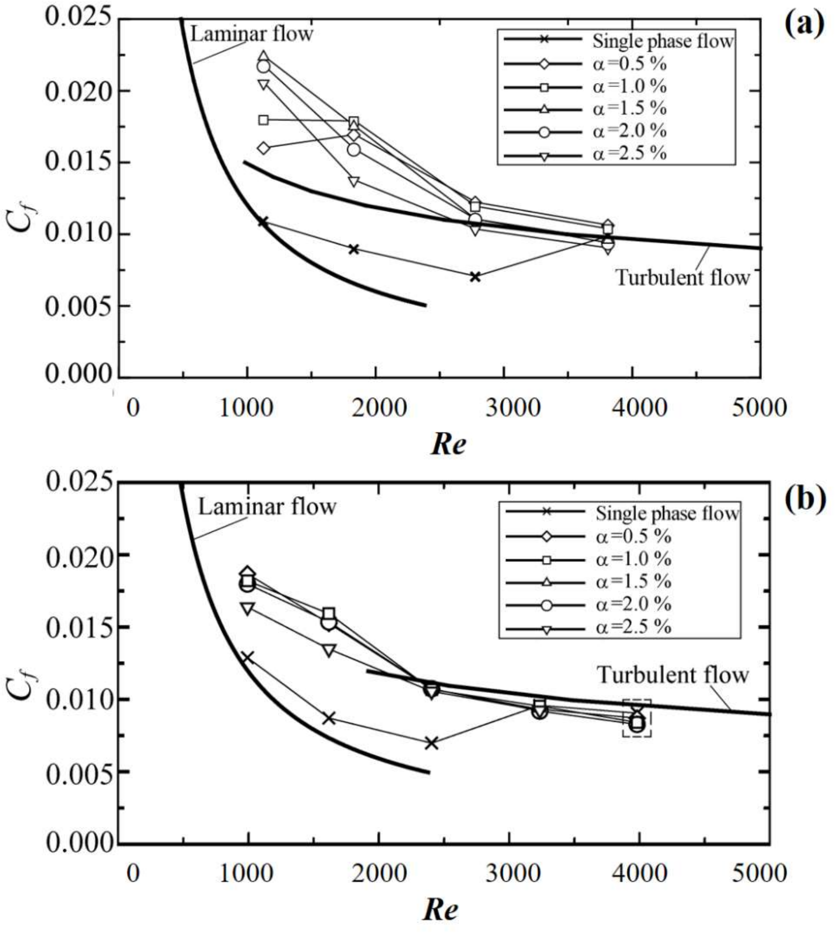

Fig. 6 Local skin-friction coefficient measured at (a) $x/H = 15$ and (b) $x/H = 45$.

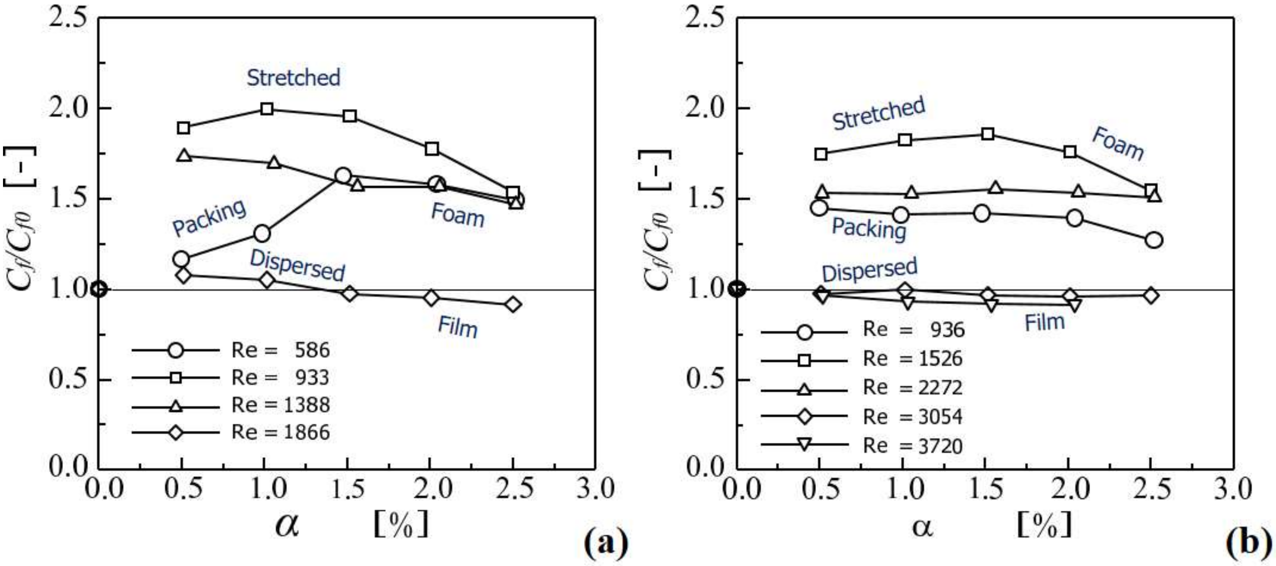

Fig. 7 Local skin-friction ratio as a function of bulk void fraction at (a) $x/H = 15$ and (b) $x/H = 45$.

The experimental result infers that two counteracting effects contribute to the modification of skin friction by bubbles. One is the high effective viscosity of the bubbly layer on the wall, which suppresses turbulence. The other is pseudo-turbulence generated by the individual motion of bubbles, which enhances turbulence. Which of these two effects dominates depends on the void fraction and Reynolds number, i.e. the nature of the bubble distribution inside the boundary layer. The ratio of the skin friction of bubby channel flow to that of single-phase flow is shown as a function of bulk void fraction in **Fig. 7**. A ratio greater than unity means an enhancement of friction, and a ratio smaller than unity means drag reduction. To ease understanding of the data, the bubble states are indicated near the corresponding plots. In the upstream region (**Fig. 7(a)**), friction was enhanced for all states except the film state. The packing state of bubbles in laminar flow increased the friction ratio by 20%–30%. This coincides with an increase in the effective viscosity of bubbles at high void fraction (Murai et al., 2016). In the foam state, the friction further rose 50% owing to the viscoelasticity of the foam layer governed by surface tension. The highest increase in friction was observed for the stretched state, which corresponds to the laminar-to-turbulent transitional region at $Re = 1866$. Under these conditions, the friction was twice that of single-phase flow. We attribute this enhancement to the pseudo-turbulence induced by actively deforming bubbles to promote an early transition to turbulent flow. Moreover, the high effective viscosity of stretched bubbles around the critical capillary number (i.e. the viscous break-up limit) contributes additional wall shear stress such that the friction overshoots the value of turbulent flow. In the downstream region (**Fig. 7(b)**), there are two differences from the upstream data. One is the increase of friction in the packing state, which means that bubble packing intensified during the long migration downstream. The other is the expansion of the drag-reduction regime at high Reynolds numbers, whereby a 9% skin-friction reduction was observed at $Re = 3722$.

3.3 *Analysis of fluctuations in wall shear stress*

Figure 8 shows the time variation of the wall shear stress in single-phase flow conditions. The ordinate is time normalized by H/U and the abscissa is normalized by the time-averaged wall shear stress. In the transition region from laminar to turbulent flow at $Re = 1866$ (**Fig. 8 (a)**), an irregular fluctuation took place owing to the intermittent passage of turbulent slugs in the channel flow. After the transition to turbulent flow at $Re = 3732$ (**Fig. 8 (b)**), the fluctuation was enhanced sharply in the positive direction. This is caused by the entrance of large sweeping structures into near wall region. By contrast, bubble injection attenuated fluctuations for both Reynolds numbers, as shown in **Fig. 9**. At $Re = 1866$, the typical time scale of the fluctuation was shortened significantly (**Fig. 9(a)**). We attribute this to the pseudo-turbulence generated by bubbles migrating in the near-wall region. At $Re = 3732$, the sharp increase of the wall shear stress disappeared in the presence of bubbles (**Fig. 9(b)**). As a result, the normalized waveform of the wall shear stress became similar for the two Reynolds numbers. This can be interpreted in one of two ways: a re-laminarization of turbulent flow with bubble injection or pseudo-turbulence causing high-frequency fluctuation in the wall shear stress.

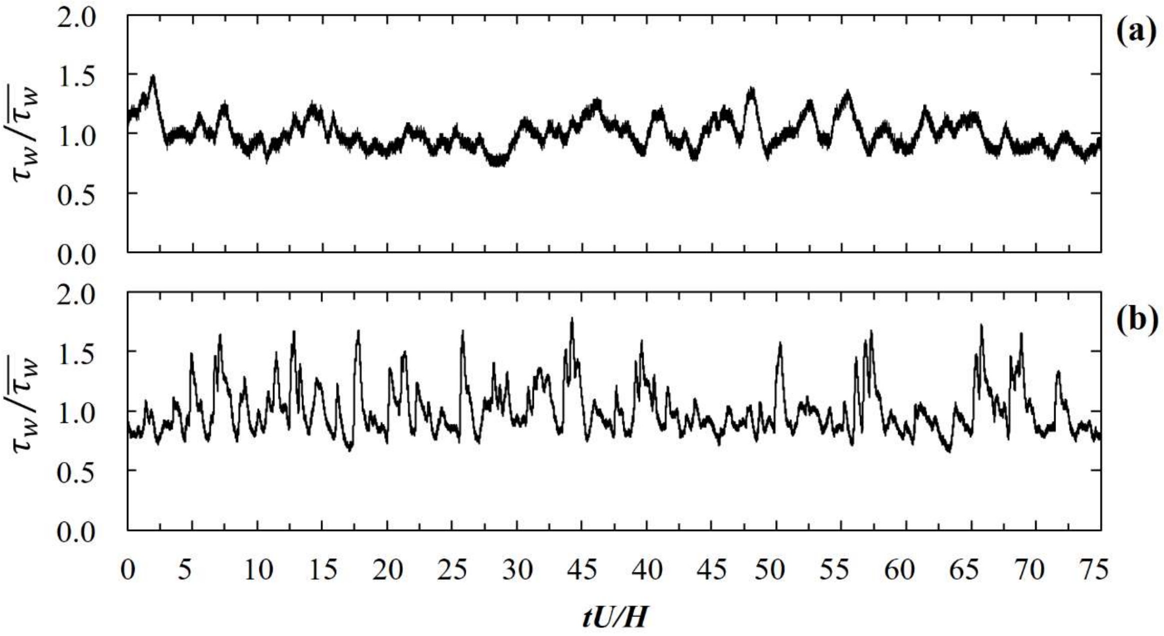

Fig. 8 Fluctuations in wall shear stress in single-phase flows at (a) $Re = 1866$ and (b) $Re = 3732$.

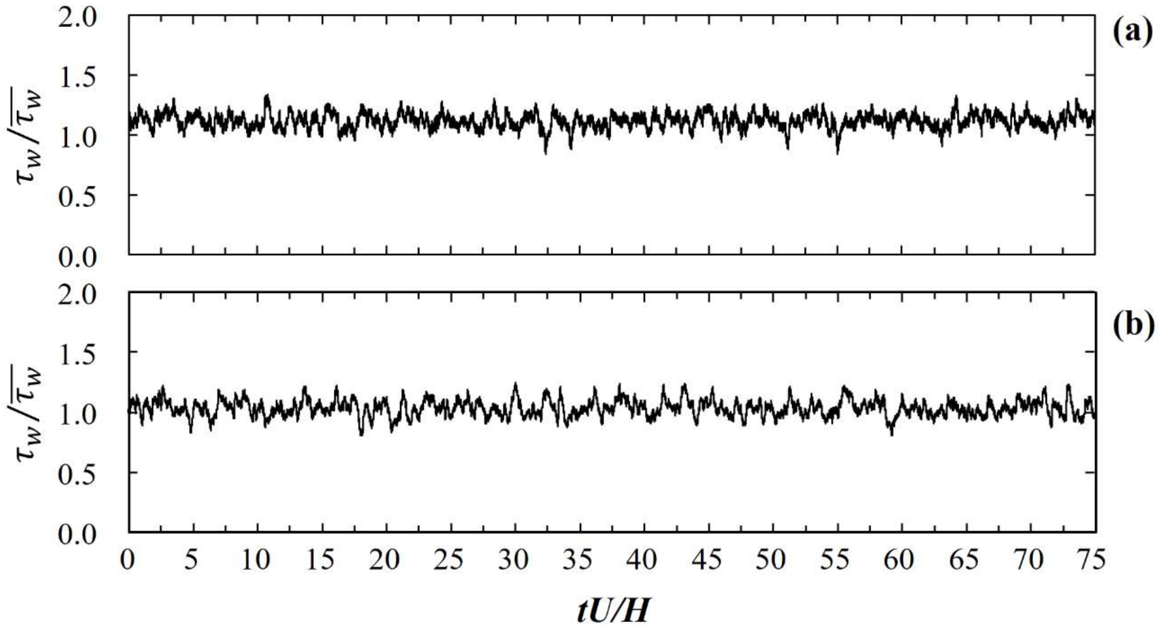

Fig. 9 Fluctuations in wall shear stress in bubbly flow at (a) $Re = 1866$ and (b) $Re = 3732$ at $\alpha = 2.0\%$.

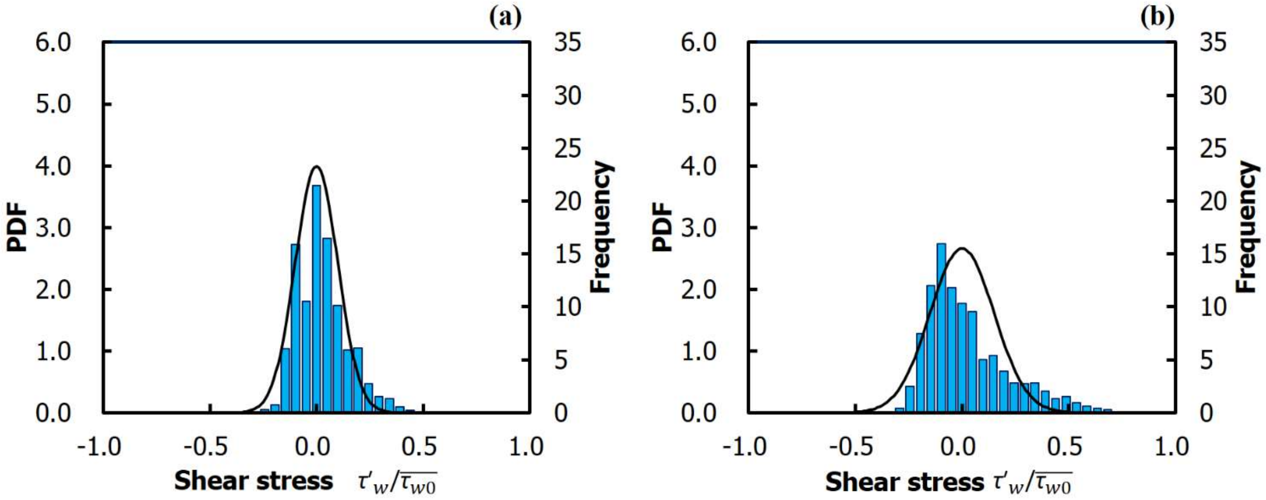

Fig. 10 Probability density distributions of fluctuations in wall shear stress in single-phase flow at (a) *Re* = 1866 and (b) *Re* = 3732. The solid curves indicate the Gaussian profiles of the corresponding average and deviation values for identifying asymmetricity of the measured fluctuations.

To quantify the effect of bubbles, we analyzed the probability density function (PDF) of the fluctuations in wall shear stress, $\tau' = \tau - \bar{\tau}_w$. **Figure 10** provides a comparison of the PDFs between two Reynolds numbers in single-phase channel flows corresponding to the fluctuations shown in **Fig. 8**. At *Re* = 1866, the PDF has a distribution similar to the Gaussian profile indicated by the solid curve (**Fig. 10(a)**). This means that the friction event happened in a random manner in the transitional region. At *Re* = 3732, the PDF has a maximum peak at a value lower than the average of the Gaussian curve, and a tail at larger values that lie well above the Gaussian profile. This corresponds to the sharp increase of the wall shear stress under turbulent flow conditions. The injection of bubbles modified the PDF, as shown in **Fig. 11**. At the lower Reynolds number, the PDF became narrower than that of the single-phase flow (Fig. 10(a)) regardless of the number of bubbles. At *Re* = 3732, the wide, asymmetric shape of the PDF for single-phase flow due to turbulence was modified into a narrower, symmetric shape, even with a small number of injected bubbles. This tended to be more pronounced as the air volume was increased. To extract the features of the PDF, we calculated the standard deviation, skewness, and kurtosis, which are plotted in **Fig. 12**.

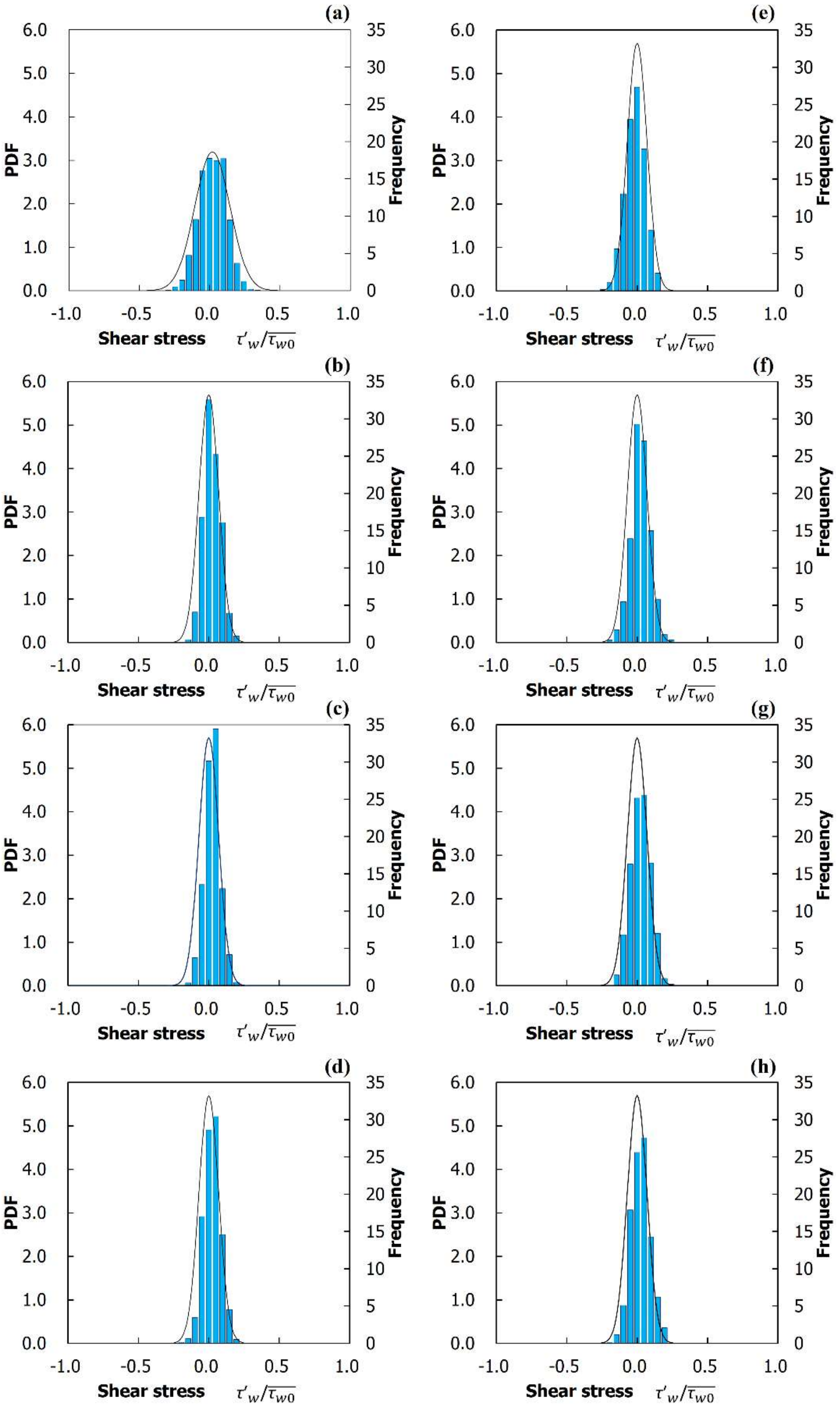

Fig. 11 Probability density distributions of fluctuations in the wall shear stress in bubbly flow under conditions of (a) $\alpha = 0.5\%$, (b) $\alpha = 1.0\%$, (c) $\alpha = 1.5\%$ and (d) $\alpha = 2.0\%$ at $Re = 1866$; and (e) $\alpha = 0.5\%$, (f) $\alpha = 1.0\%$, (g) $\alpha = 1.5\%$ and (h) $\alpha = 2.0\%$ at $Re = 3732$.

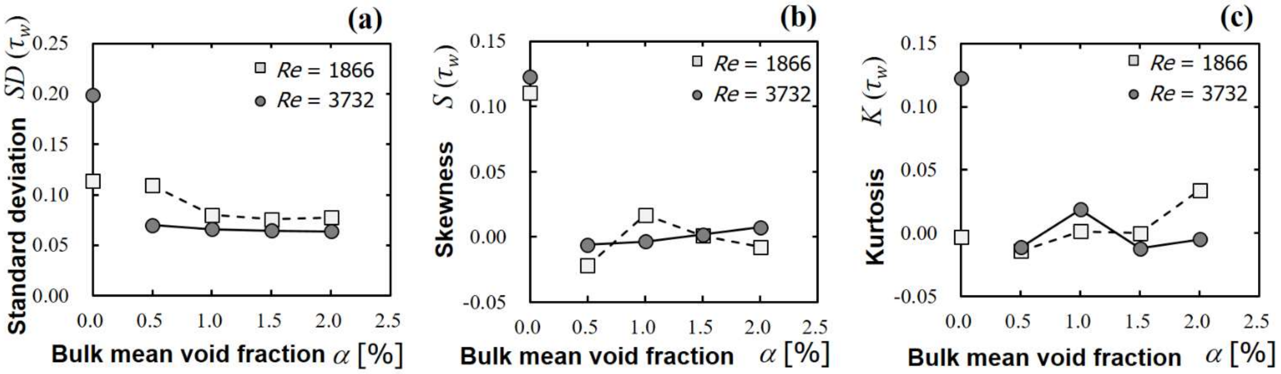

Fig. 12 Higher order moment analysis of fluctuations in the wall shear stress modified by bubbles: (a) standard deviation, (b) skewness, and (c) kurtosis.

The standard deviation at $\alpha = 0$ (**Fig. 12(a)**) was initially large at $Re = 3732$ because of the sharp increase of the wall shear stress in turbulent flow. Once bubbles were mixed ($\alpha > 0$), the deviation reduced to less than one-third of its original value. At Re =1866, in the transition region, the deviation remained almost unchanged, even with bubbles at $\alpha = 0.5\%$. An increase in void fraction reduced the deviation to a value similar to that for the case of turbulent flow. The skewness (**Fig. 12(b)**) falls to nearly zero once bubbles are introduced. Because skewness indicates the asymmetry of the event, this result infers a transition from organized flow to disorganized flow that obeys a normal random process. Thus, the original turbulent flow characteristics are changed by the injection of even a small number of bubbles. A small protrusion of the skewness at $\alpha = 1.0\%$ for $Re = 1866$ may be associated with the long stretching of bubbles observed under these conditions (see **Fig. 5**). The kurtosis (**Fig. 12(c)**) falls sharply to nearly zero at $Re = 3732$, which corresponds to the total disappearance of the spike in stress after the bubbles were introduced. By contrast, the kurtosis at $Re = 1866$ gradually increases with α. This indicates the emergence of new events inside the bubbly two-phase boundary layer in the transitional region of the channel flow. Because the time scale of the fluctuation becomes short owing to the effect of the bubbles, we can attribute all changes in the PDF moments to how bubbles move inside the boundary layer. We explain this further in the next section.

3.4 *Statistics of bubble motion*

A sample of two consecutive high-speed camera images is shown in **Fig. 13**. Using the algorithm of the PTV applied for the bubbles, we obtained individual bubble velocity vectors, as indicated by red arrows. Conducting the PTV measurement for 500 consecutive frames, we collected more than 4000 velocity vectors for statistical analysis. We note that bubbles of less than 100 μm (three pixels on the image) were ignored in the statistics.

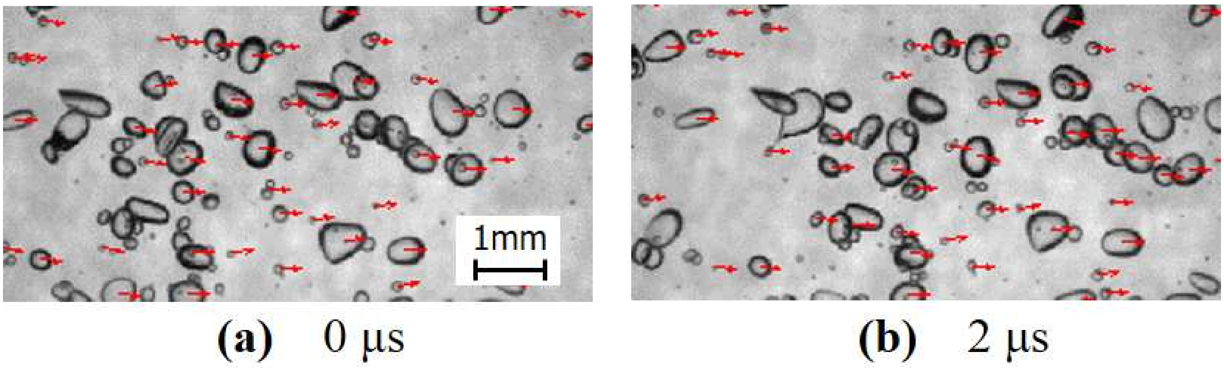

(a) 0 μs (b) 2 μs

Fig. 13 Tracking of bubbles in two consecutive frames in high-speed video images at *Re* = 3732 and α = 2.0%.

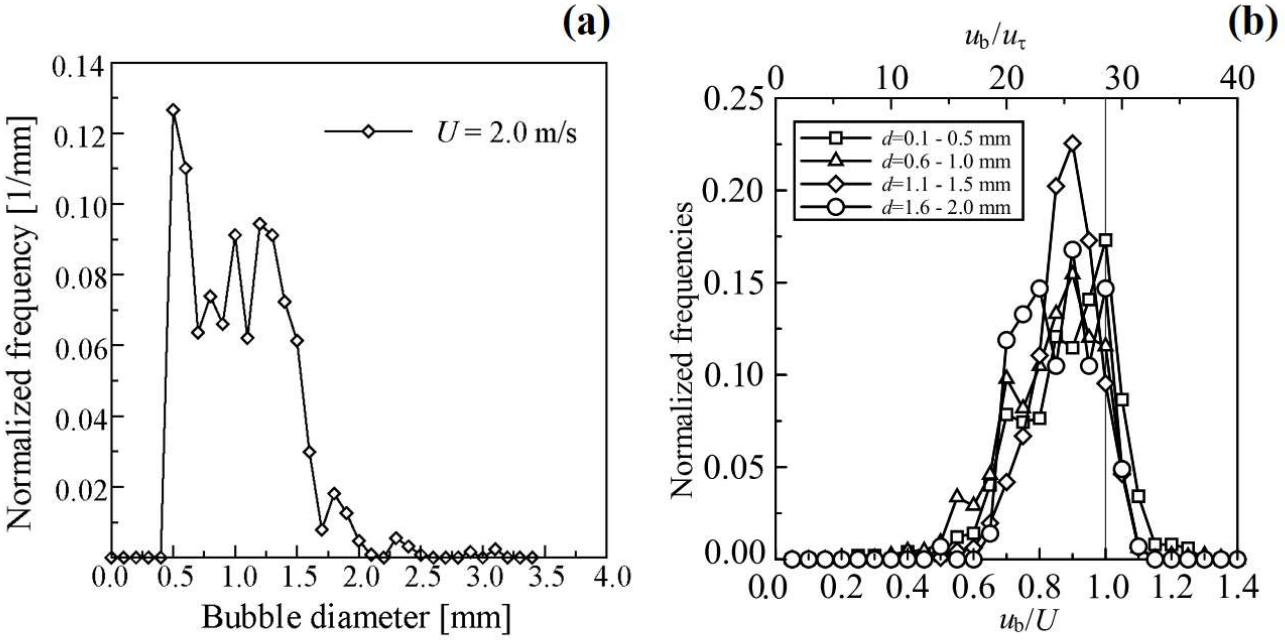

Fig. 14 Histogram of bubble motion at *Re* = 3732 at *x*/*H* = 15: (a) equivalent bubble diameter at *U* = 2.0 m/s, (b) bubble velocity distribution for different bubble diameters.

We now focus on the condition of the dispersed bubble state at *Re* = 3732 and *α* = 2.0%, at which drag reduction occurred. Figure 14(a) shows bubble size histogram defined by a sphere-equivalent diameter estimated from the pixel numbers of the individual bubbles. The histogram has several peaks in the range of 0.5 to 2.5 mm. This means fragmentation and coalescence occurred actively inside the boundary layer under a high shear rate. The maximum bubble diameter, $d_{\max}$, inside the boundary layer was estimated from the shear Weber number as

$$We_s = \frac{\rho_l d}{\sigma}\left(\frac{U}{\delta}d\right)^2 = \frac{\rho_l U^2 d^3}{\sigma \delta^2} \quad \rightarrow \quad d_{\max} = \left(\frac{\sigma\delta^2}{\rho_l U^2} We_c\right)^{1/3} = 1.1 \ \text{mm} \tag{9}$$

,

where We_c denotes the critical Weber number for fragmentation and is given by $We_c = 10$. Bubbles larger than d_{max} are seen in the histogram, which is evidence of coalescence. Because of this deviation from d_{max}, the bubble velocity had the distribution shown in **Fig. 14(b)**. The peak velocity appeared at approximately $0.9U$, and the average velocity was around $0.8U$; these velocities are slower than the liquid velocity.

In the case of water as a carrier fluid for the same liquid flow velocity, we previously measured the average bubble velocity at $0.3U$ in the wall-sliding state (Oishi et al., 2019) and approximately $0.4U$ in the dispersed state (Murai et al., 2006). Beneath a flat-bottom model ship towed at a speed of U, bubbles migrated at $0.5U$ in the void-wave state (Park et al., 2016). The bubble velocity in the present study was significantly larger than that for our previous study in water. We explain this by the silicone oil modifying the pattern of bubble motion inside the boundary layer. Namely, bubbles are stretched owing to the high viscous shear stress with low surface tension. This results in a low shear Reynolds number (Re_s):

$$Re_s = \frac{\rho_l d}{\mu_l}\left(\frac{U}{\delta}d\right), \quad \rightarrow \quad Re_{s\max} = Re_s\big|_{d=d_{\max}} = \frac{1}{\mu_l}\left(\frac{\rho_l^2 U\sigma}{\delta}We_c\right)^{1/3} . \tag{10}$$

Therefore, the capillary number of bubbles increases with the following relation

$$Ca = \frac{\mu_l}{\sigma}\left(\frac{U}{\delta}\right)d = \frac{We_s}{Re_s} . \tag{11}$$

In the silicone oil, the viscosity and surface tension are 10 times and one third that of water, respectively. On the one hand, this makes Re_s just 0.07 times the value of water; even at $U = 2.0$ m/s, Re_s is lower than 50. This implies that the bubbles behave like small bubbles dominated by viscosity and that the slip velocity from the liquid phase is restricted, resulting in high-speed migration of bubbles in the boundary layer. On the other hand, Ca is 15 times larger than in water, which leads to bubble deformability, as is the case for large bubble in water. At $U = 2.0$ m/s, Ca exceeds 0.2 and belongs to the large shear-deformation regime, where the bubbles' surface area increases to interact with surrounding turbulent eddies. The combination of these two conditions creates intrinsic motion of bubbles in silicone oil that is different from that in water. We therefore attribute the high-speed migration of the bubbles to the effects of low Re_s and high Ca; that is, small but deformable bubbles attenuate turbulence with their shape oscillation adjusted to local coherent structures.

3.5 *Relationship between wall shear stress and local void fraction*

In this section we analyze the mechanism of interaction between bubbles and local wall shear stress. **Figure 15** shows the results of the synchronized measurement of the wall shear stress and projection void fraction, taken at $\alpha = 2.0\%$ and $Re = 3732$. Under these conditions, drag reduction was observed. The upper picture is the corresponding bubble image for the same sampling period (**Fig. 15(a)**). In **Fig. 15(b)**, there is a large temporal fluctuation in the wall shear stress that corresponds to a fluctuation in void fraction fluctuates. The wall shear stress reaches a local minimum value before the void fraction reaches a local maximum value. This means that drag reduction does not occur simultaneously with the increase in void fraction, but is promoted by the void fraction with a slight time lag. Park et al. (2016) found spontaneous generation of void waves in a flat-bottom model ship when drag reduction occurred. They derived a wave equation of the void fraction from two-fluid model equations applied for the turbulent boundary layer. Their derivation highlights the importance for drag reduction in the spatial gradient of the void fraction:

$$\tau_w = \tau_{w0}\left(1 - G_1\alpha - G_2\frac{\partial\alpha}{\partial x}\right), \tag{12}$$

where G_1 is the gain factor to the instantaneous void fraction and G_2 is the gain factor to spatial gradient of the void fraction. For our data, the spatial gradient is shown in **Fig. 15 (c)**. The waveform of the spatial gradient is similar to that of the fluctuation in wall shear stress with a time lag.

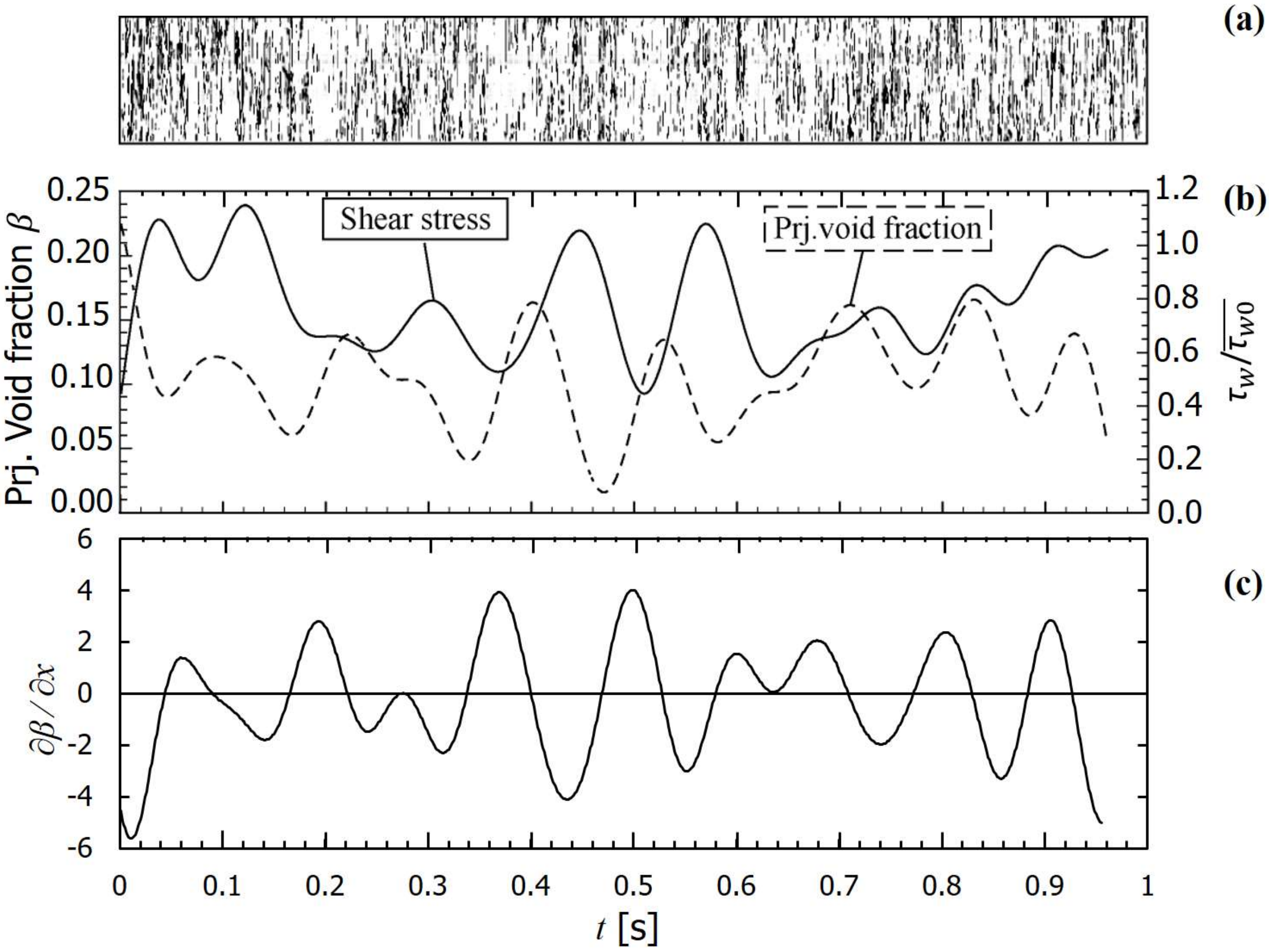

Fig. 15 Temporal relationship between the wall shear stress and projection void fraction at $Re = 3732$ ($U = 2.0$ m/s) and $x/H = 45$. (a) Timeline image taken at the measurement location. (b) Variation of the local skin friction and the local projection void fraction obtained in synchronized measurements. (c) Spatial gradient of the projected void fraction estimated from time derivative of the void faction and the averaged velocity of bubble migration.

To quantify the time lag, cross-correlation between the wall shear stress and the projection void fraction was analyzed with a variable time lag, Δt. The result is depicted in **Fig. 16**. At $\Delta t = 0$, the cross-correlation, C, has a value close to zero. This indicates that the two quantities are mostly in orthogonal relation to each other. There are two kinds of time shift present in the results, at which the correlation has local peak values. One is $\Delta t_1 = -0.04$ s for $C = 0.6$, and the other is $\Delta t_2 = 0.08$ s for $C = 0.5$, which correspond to $\Delta x_1 = -0.08$ m and $\Delta x_2 = 0.16$ m in space lag, respectively.

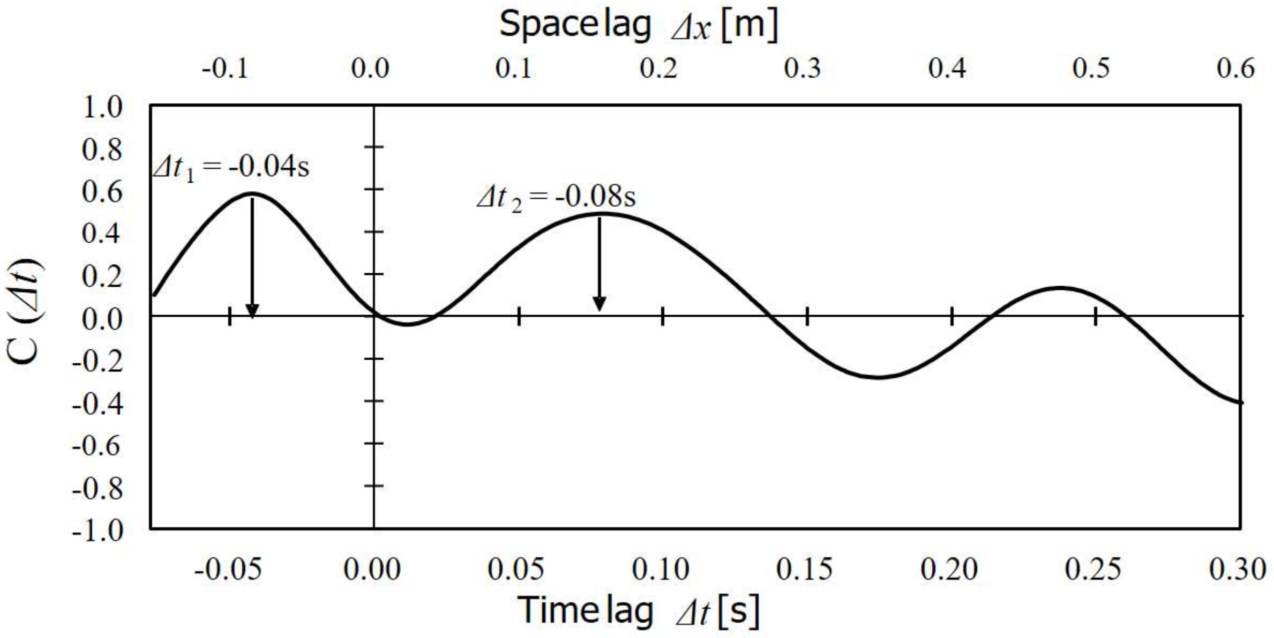

Fig. 16 Cross-correlation between the wall shear stress and the projection void fraction.

We explain below the factors that determine the time lag. One of candidate time scales that matches the time lag is the resonant period of free bubble deformation in liquid (Feng and Leal, 1997) given by

$$t_d = \frac{\pi}{\sqrt{2(n-1)(n+1)(n+2)}}\sqrt{\frac{\rho d^3}{\sigma}}, \tag{13}$$

where n is the mode number of the shape deformation. On the elliptic oscillation at $n = 2$, which is a typical condition of bubbles (e.g. $d = 5$ mm) in the present experiment, yields

$$t_d = \frac{\pi}{\sqrt{2 \times 1 \times 3 \times 4}}\sqrt{\frac{10^3 \times (0.005)^3}{0.02}} = 0.05 \ \ \text{s.} \tag{14}$$

Hence, the time scale of deformation and the measured time lag have the same order. If this is the cause of the time lag of void-to-drag relation, it means that bubbles in a swarm are harmoniously and periodically deformed. Using a typical observed wavelength of the fluctuation in void fraction, $\lambda = 0.13$ s × 2.0 m/s = 0.26 m, the value of G_2 in Eq. (12) for our silicone-oil channel flow is estimated as

$$\sin\varphi = \frac{-2\pi G_2/\lambda}{\sqrt{G_1^2 + \left(2\pi G_2/\lambda\right)^2}} = \sin\left(\frac{0.05}{0.13}\right) = 0.66, \qquad \rightarrow G_2 = 0.16G_1, \tag{15}$$

where φ is the phase shift of the wall shear stress from the void fraction fluctuation.

Another candidate factor we need to consider is the fluctuation of the effective viscosity in the dense bubbly layer. In a steady linear shear flow, the effective viscosity of the bubbly liquid is given approximately by

$$\mu = \mu_0 \exp\left(\frac{A\alpha}{1-k\alpha}\right) = 1 + A\alpha + \frac{1}{2}A\left(A+2k\right)\alpha^2 + O(\alpha^3), \tag{16}$$

where μ_0 is the liquid viscosity without bubbles. The value of the constant, A, is $A = 1$ for clean bubbles, and $A = 5/2$ for contaminated bubbles or solid particles. The factor k is determined by the spatial arrangement of bubbles, and is within the range of $1.35 < k < 1.91$, in accordance with the two limits between a face-centered cubic lattice and simple cubic arrangement. Inside the bubble swarm, the local void fraction, α, easily approaches its packing limit to reduce $1-k\alpha$ in Eq. (16) to nearly zero. This exponentially raises the effective viscosity to several hundred times the liquid viscosity (experimentally proven by Murai et al. 2015 for a circular Couette flow). The turbulence in such bubble swarms is suppressed, which results in a reduction of wall shear stress. The time lag between the change of the effective viscosity and turbulence suppression is scaled by

$$t_v = \frac{\delta^2}{\nu} = \frac{\rho\delta^2}{\mu_0}\exp\left(-\frac{A\alpha}{1-k\alpha}\right), \tag{17}$$

where δ and ν are the boundary-layer thickness and kinematic viscosity (defined by the effective viscosity), respectively. Using the experimental conditions and the measured time lag, Eq. (17) gives an estimate of the local void fraction in bubble swarms as

$$\alpha = \frac{1}{k + A\log\left(\dfrac{\rho\delta^2}{t_v\mu_0}\right)} \cong \frac{1}{1.5 + 1\cdot\log\left(\dfrac{10^3\times 0.005^2}{0.05\times 10^{-3}}\right)} \cong 0.13\cdot \tag{18}$$

This value matches the average value of the boundary layer void fraction. Therefore, the role of the effective viscosity on the lag time remains as one of the governing factors.

These two factors (i.e. the transiency of bubble deformation and the effective viscosity transferred to the wall) combine in the bubbly two-phase boundary layer. The theory just gives a primary order estimation and needs to be proved by a wide range of parametric studies in the future. Nevertheless, at this stage, we are able to attribute the fluctuation in the wall shear stress to the unsteadiness of bubble deformation, which is a feature in silicone-oil channel flow.

4. Conclusions

We performed laboratory experiments on bubbly channel flows using silicone oil (which has a lower surface tension than water and a clean interface to bubbles) to evaluate quantitatively the wall shear stress for various regimes in the bubble motion. We visualized bubbles using a high-speed video camera and time-series measurements of the wall shear stress using a wall shear stress sensor. This allowed us to classify different patterns of bubble deformation and swarms in the channel, and to correlate these patterns with modifications of wall shear stress. The patterns were classified as packing, film, foam, dispersed, and stretched states. The wall shear stress decreased in the dispersed and film states by 9% from the single-phase condition, whereas it increased in the stretched, packing, and foam states. Statistical analysis of the wall shear stress was carried out for two typical Reynolds numbers corresponding to the transition and turbulent regimes. Variations in the shape of the PDF of the wall shear stress and the higher order moments indicated the generation of pseudo-turbulence in the transition regime and suppression of the drag-inducing events in the turbulent regime as a result of bubble injection. Simultaneous measurement of bubble images and the wall shear stress allowed us to correlate the local void fraction (representing advection of the bubble swarm) and the wall shear stress, revealing a time lag between the fluctuations in these two local quantities. Based on bubble dynamics and the effective viscosity of bubble dispersions, two kinds of time scale likely to explain the measured time lag were proposed as a feature of the bubbly two-phase boundary layer in silicone oil as the liquid phase.

Acknowledgements

Funding: This research was supported by the Japan Society for Promotion of Science (JSPS KAKENHI) [grant numbers 17H01245, 20K04255].

References

Agrawal, R., Ng, H.C.-H., Dennis, D.J.C., Poole, R.J., 2020. Investigating channel flow using wall shear stress signals at transitional Reynolds numbers. Int. J. Heat Fluid Flow 82, 108525. https://doi.org/10.1016/j.ijheatfluidflow.2019.108525

Aoyama, S., Hayashi, K., Hosokawa, S., Tomiyama, A., 2018. Shapes of single bubbles in infinite stagnant liquids contaminated with surfactant. Exp. Thermal Fluid Sci. 96, 460–469. https://doi.org/10.1016/j.expthermflusci.2018.03.015

Asiagbe, K.S., Fairweather, M., Njobuenwu, D.O., Colombo, M., 2017. Large eddy simulation of microbubble transport in a turbulent horizontal channel flow. Int. J. Multiphase Flow 94, 80–93. https://doi.org/10.1016/j.ijmultiphaseflow.2017.04.016

Ceccio, S.L., 2010. Friction drag reduction of external flows with bubble and gas injection. Annu. Rev. Fluid Mech. 42, 183–203. https://doi.org/10.1146/annurev-fluid-121108-145504

Chahed, J., Bellakhel, G., Kanfoudi, H., 2017. Bubbles' slip velocity reduction in the near wall region of turbulent bubbly pipe flows under different gravity conditions. Chem. Eng. Res. Des. 119, 231–244. https://doi.org/10.1016/J.CHERD.2017.01.015

Colombo, M., Fairweather, M., 2016. RANS simulation of bubble coalescence and break-up in bubbly two-phase flows. Chem. Eng. Sci. 146, 207–225. https://doi.org/10.1016/J.CES.2016.02.034

Dean, R., 1978, Reynolds Number Dependence of Skin Friction and Other Bulk Flow Variables in Two-Dimensional Rectangular Duct Flow, J. Fluids Eng. 100, 215–223. https://doi.org/10.1115/1.3448633

Du Cluzeau, A., Bois, G., Toutant, A., 2019. Analysis and modelling of Reynolds stresses in turbulent bubbly up-flows from direct numerical simulations. J. Fluid Mech. 866, 132–168. https://doi.org/10.1017/jfm.2019.100

Esmaeeli, A., Tryggvason, G., 1996. An inverse energy cascade in two-dimensional low Reynolds number bubbly flows. J. Fluid Mech. 314, 315–330. https://doi.org/10.1017/S002211209600033X

Feng, J., Bolotnov, I.A., 2017. Interfacial force study on a single bubble in laminar and turbulent flows. Nucl. Eng. Des. 313, 345–360. https://doi.org/10.1016/J.NUCENGDES.2016.12.034

Feng, Z. C., Leal, L. G., 1997. Nonlinear bubble dynamics, Annu. Rev. Fluid Mech. 29, 201–243.

Ferrante, A., Elghobashi, S., 2007. On the effects of microbubbles on Taylor–Green vortex flow. J. Fluid Mech. 572, 145–177. https://doi.org/10.1017/S0022112006003545

Ferrante, A., Elghobashi, S., 2005. Reynolds number effect on drag reduction in a microbubble-laden spatially developing turbulent boundary layer. J. Fluid Mech. 543, 93–106. https://doi.org/10.1017/S0022112005006440

Ferrante, A., Elghobashi, S., 2004. On the physical mechanisms of drag reduction in a spatially developing turbulent boundary layer laden with microbubbles. J. Fluid Mech. 503, 345–355. https://doi.org/10.1017/S0022112004007943

Ferrante, A., Elghobashi, S., 2003. On the physical mechanisms of two-way coupling in particle-laden isotropic turbulence. Phys. Fluids 15, 315–329. https://doi.org/10.1063/1.1532731

Fukuta, M., Takagi, S., Matsumoto, Y., 2008. Numerical study on the shear-induced lift force acting on a spherical bubble in aqueous surfactant solutions. Phys. Fluids 20, 040704. https://doi.org/10.1063/1.2911040

Hao, W.U., Yongpeng, O.U., 2019. Numerical simulation of air layer morphology on flat bottom plate with air cavity and evaluation of the drag reduction effect. Int. J. Nav. Archit. Ocean Eng. https://doi.org/10.1016/j.ijnaoe.2018.09.005

Iwata, R., Takeuchi, S., Kajishima, T., 2010. Large-scale analysis of interactive behaviors of bubbles and particles in a liquid by a coupled immersed boundary and VOF technique. Multiphase Sci. Technol. 22, 233–246. 10.1615/MultScienTechn.v22.i3.40

Joshi, J.B., Nandakumar, K., Evans, G.M., Pareek, V.K., Gumulya, M.M., Sathe, M.J., Khanwale, M.A., 2017. Bubble generated turbulence and direct numerical simulations. Chem. Eng. Sci. 157, 26–75. https://doi.org/10.1016/j.ces.2016.03.041

Kawamura, T., Kodama, Y., 2002. Numerical simulation method to resolve interactions between bubbles and turbulence. Int. J. Heat Fluid Flow 23, 627–638. https://doi.org/10.1016/S0142-727X(02)00158-3

Kim, J., Moin, P., Moser, R., 1987. Turbulence statistics in fully developed channel flow at low Reynolds number. J Fluid Mech. 177, 133–166. https://doi.org/10.1017/S0022112087000892

Kodama, Y., Kakugawa, A., Takahashi, T., Kawashima, H., 2000. Experimental study on microbubbles and their applicability to ships for skin friction reduction. Int. J. Heat Fluid Flow 21, 582–588. https://doi.org/10.1016/S0142-727X(00)00048-5

Lin, S., Lu, J., Tryggvason, G., Zhang, Y., 2019. The effect of fluid shear on oscillating bubbly flows. Phys. Fluids 31. https://doi.org/10.1063/1.5089664

Lu, J., Tryggvason, G., 2007. Effect of bubble size in turbulent bubbly downflow in a vertical channel. Chem. Eng. Sci. 62, 3008–3018. https://doi.org/10.1016/j.ces.2007.02.012

Ma, M., Lu, J., Tryggvason, G., 2016. Using statistical learning to close two-fluid multiphase flow equations for bubbly flows in vertical channels. Int. J. Multiphase Flow 85, 336–347. https://doi.org/10.1016/j.ijmultiphaseflow.2016.06.021

McCormick, M.E., Bhattacharyya, R., 1973. Drag reduction of A submersible hull by electrolysis. Nav. Eng. J. 85, 11–16. https://doi.org/10.1111/j.1559-3584.1973.tb04788.x

Murai, Y., 2014. Frictional drag reduction by bubble injection. Exp. Fluids 55, 1773. https://doi.org/10.1007/s00348-014-1773-x

Murai, Y., Fukuda, H., Oishi, Y., Kodama, Y., Yamamoto, F., 2007. Skin friction reduction by large air bubbles in a horizontal channel flow. Int. J. Multiphase Flow 33, 147-163.Murai, Y., Matsumoto, Y., Yamamoto F., 2001, Three-dimensional measurement of void fraction in a bubble plume using statistic stereoscopic image processing, Exp. Fluids 30, 11–21. https://doi.org/10.1007/s003480000129

Murai, Y., Oishi, Y., Takeda, Y., Yamamoto, F., 2006. Turbulent shear stress profiles in a bubbly channel flow assessed by particle tracking velocimetry, Exp. Fluids. 41, 2, 343–352. https://doi.org/10.1007/s00348-006-0142-9

Murai, Y., Oiwa, H., 2008. Increase of effective viscosity in bubbly liquids from transient bubble deformation. Fluid Dyn. Res. 40, 565–575. https://doi.org/10.1016/j.fluiddyn.2007.12.009

Murai, Y., Shiratori, T., Kumagai, I., Rühs, P.A., Fischer, P., 2015. Effective viscosity measurement of interfacial bubble and particle layers at high volume fraction. Flow Meas. Instrum. 41, 121–128. https://doi.org/10.1016/j.flowmeasinst.2014.10.006

Oishi, Y., Tohge, Y., Tasaka, Y., Murai, Y., 2019. Bubble clustering in a horizonal turbulent channel flow investigated by bubble-tracking velocimetry. Int. J. Multiphase Flow 120, 103104.

Pang, M., Zhang, Z., 2018. Numerical investigation on turbulence drag reduction by small bubbles in horizontal channel with mixture model combined with population balance model. Ocean Eng. 162, 80–97. https://doi.org/10.1016/J.OCEANENG.2018.05.034

Pang, M.J., Wei, J.J., Yu, B., 2017. Investigation on Effect of Gravity Level on Bubble Distribution and Liquid Turbulence Modification for Horizontal Channel Bubbly Flow. Microgravity Sci. Technol. 29, 313–324. https://doi.org/10.1007/s12217-017-9549-6

Pang, M.J., Wei, J.J., Yu, B., 2014. Numerical study on modulation of microbubbles on turbulence frictional drag in a horizontal channel. Ocean Eng. 81, 58–68. https://doi.org/10.1016/j.oceaneng.2014.02.012

Park, H.J., Oishi, Y., Tasaka, Y., Murai, Y., 2016. Void waves propagating in the bubbly two-phase turbulent boundary layer beneath a flat-bottom model ship during drag reduction. Exp. Fluids 57, 178. https://doi.org/10.1007/s00348-016-2268-8

Park, H.J., Tasaka, Y., Murai, Y., 2018. Bubbly drag reduction accompanied by void wave generation inside turbulent boundary layers. Exp. Fluids 59, 166. https://doi.org/10.1007/s00348-018-2621-1

Park, H.J., Tasaka, Y., Murai, Y., 2019. Bubbly drag reduction investigated by time-resolved ultrasonic pulse echography for liquid films creeping inside a turbulent boundary layer. Exp. Thermal Fluid Sci. 103, 66–77. https://doi.org/10.1016/j.expthermflusci.2018.12.025

Rust, A.C., Manga, M., 2002. Effects of bubble deformation in the viscosity of dilute suspensions. J. Non-Newtonian Fluid Mech. 104, 53–63. https://doi.org/10.1016/S0377-0257(02)00013-7

Parkinson, L., Sedev, R., Fornasiero, D., Ralston, J., 2008. The terminal rise velocity of 10-100 μm diameter bubbles in water. J. Colloid Interface Sci. 322, 168–172. https://doi.org/10.1016/j.jcis.2008.02.072

Rawat, S., Chouippe, A., Zamansky, R., Legendre, D., Climent, E., 2019. Drag modulation in turbulent boundary layers subject to different bubble injection strategies. Comput. Fluids 178, 73–87. https://doi.org/10.1016/J.COMPFLUID.2018.09.011

Roghair, I., Lau, Y.M., Deen, N.G., Slagter, H.M., Baltussen, M.W., Van Sint Annaland, M., Kuipers, J.A.M., 2011. On the drag force of bubbles in bubble swarms at intermediate and high Reynolds numbers. Chem. Eng. Sci. 66, 3204–3211. https://doi.org/10.1016/j.ces.2011.02.030

Sanders, W, C,, Winkel, E. S., Ceccio, S. L., 2006. Bubble friction drag reduction in a high-Reynolds number flat-late turbulent boundary layer. J. Fluid Mech. 552, 353–380. https://doi.org/10.1017/S0022112006008688

Seo, J.H., Lele, S.K., Tryggvason, G., 2010. Investigation and modeling of bubble-bubble interaction effect in homogeneous bubbly flows. Phys. Fluids 22, 1–18. https://doi.org/10.1063/1.3432503

Sugiyama, K., Calzavarin, E., Lohse, D., 2008. Microbubbly drag reduction in Taylor-Couette flow in the wavy vortex regime. J. Fluid Mech. 608, 21–41. https://doi.org/10.1017/S0022112008001183

Takagi, S. Matsumoto, Y., 2011. Surfactant effects on bubble motion and bubbly flows. Annu. Rev. Fluid Mech. 43, 615–636. https://doi.org/10.1146/annurev-fluid-122109-160756

Tasaka, Y., Kimura, T., Murai, Y., 2015. Estimating the effective viscosity of bubble suspensions in oscillatory shear flows by means of ultrasonic spinning rheometry. Exp. Fluids 56, 1867. https://doi.org/10.1007/s00348-014-1867-5

Vreman, A.W., Kuerten, J.G.M., 2014. Statistics of spatial derivatives of velocity and pressure in turbulent channel flow. Phys. Fluids 26, 085103. https://doi.org/10.1063/1.4891624

Winkel, E. S., Ceccio, S. L., Dowling, D. R., Perlin, M., 2004. Bubble-size distributions produced by wall injection of air into flowing freshwater, saltwater and surfactant solutions. Exp. Fluids 37, 802–810. https://doi.org/10.1007/s00348-004-0850-y

Zhang, X., Wang, J., Wan, D., 2020. Euler-Lagrange study of bubble drag reduction in turbulent channel flow and boundary layer flow. Phys. Fluids 32, 027101. https://doi.org/10.1063/1.5141608

Zhang, Z., Legendre, D., Zamansky, R., 2019. Model for the dynamics of micro-bubbles in high-Reynolds-number flows. J. Fluid Mech. 879, 554–578. https://doi.org/10.1017/jfm.2019.662

Zhao, X., Zong, Z., Jiang, Y., Pan, Y., 2019. Numerical simulation of micro-bubble drag reduction of an axisymmetric body using OpenFOAM. J. Hydrodyn. 31, 900–910. https://doi.org/10.1007/s42241-018-0118-2